A&A 387, 744–757 (2002)
DOI: 10.1051/0004-6361:20020389

Astronomy & Astrophysics

Restoration of interferometric images

II. The case-study of the Large Binocular Telescope

M. Carbillet[1], S. Correia[2,3], P. Boccacci[4], and M. Bertero[4]

[1] Osservatorio Astrofisico di Arcetri, largo E. Fermi 5, 50125 Firenze, Italy
[2] UMR 6525 Astrophysique, Université de Nice–Sophia Antipolis, Parc Valrose, 06108 Nice Cedex 2, France
[3] European Southern Observatory, Alonso de Cordova 3107, casilla 19001, Santiago 19, Chile
e-mail: scorreia@eso.org
[4] INFM and DISI, Università di Genova, via Dodecaneso 33, 16146 Genova, Italy
e-mail: boccacci@disi.unige.it; bertero@disi.unige.it

Received 13 February 2002 / Accepted 8 March 2002

Abstract. We present in this paper a study of the imaging properties of the Large Binocular Telescope interferometer, focusing our attention on what we believe to be the most relevant effects, namely the limited angular coverage and the partial adaptive optics (AO) correction. For this purpose we make use of the Software Package AIRY (Astronomical Image Restoration in interferometrY), designed for multiple deconvolution of interferometric images and presented in our previous paper. We also consider as our testing object a model of young binary star consisting of a core binary surrounded by a massive circumbinary ring seen in scattered light, similar to that of GG Tau. The effect of angular coverage, linked to the problem of time-averaging smearing of the interferometric images, is investigated for a number of cases corresponding to different declinations of the observed object. We find encouraging results showing that a good estimation of the relevant astronomical parameters of the object can be obtained even with an incomplete angular coverage. We then study the effect of partial AO-correction for both schemes of classical AO and multi-conjugate AO. We show that uniformity of the point-spread function over the field-of-view, rather than absolute global quality, is fundamental for the quality of the restored image.

Key words. instrumentation: interferometers – instrumentation: adaptive optics – techniques: interferometric – techniques: image processing – methods: numerical – stars: imaging

1. Introduction

In a previous paper, hereafter referred to as Paper I (Correia et al. 2002), we present the Software Package AIRY (Astronomical Image Restoration in interferometrY) designed for the simulation and restoration of the images of LBT (Large Binocular Telescope) and LBT-like interferometers (as for example the 20/20 telescope project). The main peculiarity of this kind of interferometers is the possibility of getting a good coverage of the u–v spatial frequency plane by means of a few observations at different orientations of the baseline with respect to the sky (i.e. different parallactic angles). Indeed LBT is a two 8.4 m pupils interferometer with a center-to-center baseline of 14.4 m, both pupils being placed on a common alt-azimuthal mount.

The associated restoration problem is that a unique high-resolution image of the astronomical target will have to be recovered from a set of interferometric observations corresponding to different parallactic angles. Several restoration methods can be applied to this problem (see, for instance, Bertero & Boccacci 2000b). In the present paper we use the iterative method known as OS-EM (Ordered Subsets – Expectation Maximization), proposed in Bertero & Boccacci (2000a), and implemented within the Software Package AIRY (see Paper I). It is an accelerated version of the EM (Expectation Maximization) method (Shepp & Vardi 1982), also known in astronomy as the LR (Lucy-Richardson) method.

The purpose of this paper is to study the peculiar interferometric imaging performance of LBT by means of numerical simulations. In particular, we study what we have identified to be the most relevant effects, namely the limitation in angular coverage, and the partial AO-correction.

As concerns the angular coverage, it must be observed that, due to the alt-azimuthal mount of the telescope, the effects of earth rotation during the night are both a rotation of the field and a rotation of the projection of the baseline onto the object. The first rotation is compensated by a hardware device (a field de-rotator), while the second one is used to sample the u–v plane.

Send offprint requests to: M. Carbillet,
e-mail: marcel@arcetri.astro.it

Since the variation of the parallactic angle with time is a non-uniform function of the object declination, the implication is twofold. First, the range of parallactic angles accessible during the night can be limited (i.e. less than 180°), depending on the object declination. The consequence is an incomplete coverage of the u–v plane. Second, and due to the variation of the fringe pattern rotation rate during the night, the variation of parallactic angle during the integration time is not negligible in some circumstances – when the object is close to the zenith for instance – so that, for a given integration time, it can induce significant differences in angular range for different baseline orientations.

As concerns partial AO-correction, we recall that, in the case of LBT, a high-level AO system is intended to correct for the atmospheric turbulence effects on each pupil, directly on the secondary mirror, and to cophase each beam before recombination. LBT first light, including an adaptive optics (AO) system based on adaptive secondary mirrors and pyramid wavefront sensors, is planned for early 2004. The final AO system will also include multi-conjugate (MC) AO features, intended to achieve high-quality correction on a wide field-of-view (FoV). A broad range of image quality can anyway be achieved, mainly due to variation of the seeing conditions, but also to a series of other factors as the number of photons that are allowed for wavefront sensing and the angular distance between the AO guide star and the astronomical target. Hence the study of such an effect on the restored image appears to be a fundamental issue.

The above mentioned effects are investigated by simulating high-resolution LBT interferometric observations of an astronomical object of interest, and comparing the scientific parameters of the restored object with the original ones. From this point of view the present work is to be considered as the continuation of preliminary studies already presented elsewhere (Correia et al. 2000; Carbillet et al. 2000; Correia et al. 2001), as well as in Paper I.

All along this study we use as astronomical object a model of young binary star consisting of a core binary surrounded by a dusty circumbinary ring. The model is directly inspired by near-infrared observations of the famous T-Tauri binary star of the quadruple system GG Tau and their consecutive data interpretation/modelization (Roddier et al. 1996; Wood et al. 1999). We believe that this type of object is challenging for any kind of restoration method because it combines point-like features (the core binary star) and a diffuse one (the circumbinary ring), with a high-dynamic range between them. For a better understanding of the capabilities of the restoration method as well as of the effects due to the above mentioned features, we also treat separately the two components of the object. We first look at the detectability of both the core binary star and the circumbinary ring, and then we quantify the quality of the reconstruction: for the core binary star we compute the error on the reconstruction of its astrometric and photometric parameters while, for the circumbinary ring we evaluate the error on some suitable morphological parameters.

The paper is organized as follows. In Sect. 2 we describe in detail the model of astronomical object considered for our study, as well as the general features of the sets of PSFs used and the associated imaging process. In Sect. 3 we describe our simulation of observations corresponding to different declinations of the astronomical object (and then to different amounts of angular coverage), and give the results obtained by applying the restoration method to the various sets of observations. The relevant scientific parameters are plotted as functions of the number of OS-EM iterations and the features of the restorations are discussed. The effect of the quality of the attained AO correction is studied in Sect. 3.3, for both cases of classical AO and MCAO. In Sect. 5 we summarize the results of the paper and give our conclusions.

2. The simulated data

2.1. The astronomical object: A model of young binary star

We assume as our astronomical object a young binary star with scattered light emission coming from the presence of a dusty circumbinary ring. The model is produced using observational parameters for the ring emission taken from observations of the close binary of the quadruple GG Tau system obtained in the near-infrared by Roddier et al. (1996), and reproduced afterwards in modelizations by Wood et al. (1999). According to the latter we assume that:

1. the light scattered by the circumbinary ring is mainly contained within two concentric ellipses with the same axial ratio $b/a = 0.82$ and with semi-major axes of, respectively, ∼10 and ∼20 times the binary angular separation ρ;
2. the ratio between scattered and direct light in K-band is 0.57×10^{-2} (corresponding to a difference of integrated magnitude between the core binary star and the circumbinary ring of ∼5.64 mag);
3. the ratio of scattered light between the near side and the far side of the ring is ∼2.

In addition, the ring inclination angle is set to 35° and lumpy features are included. As concerns the binary star lying in the core of the dynamically cleared region, we assume an angular separation ρ twice the angular resolution limit of LBT in K-band (i.e. ∼40 mas), and a position angle PA chosen in such a way that the position of the companion star *does not* coincide with a given pixel. We also assume a main component K-magnitude $m = 10$ and a difference of magnitude $\Delta m = 1$. We point out that the brightness of the central binary we consider here is sufficiently realistic for this type of object (see for instance Ghez et al. 1997) and leads to a ring integrated magnitude of ∼15.25 (i.e. 15.48 mag/arcsec^2). This model could

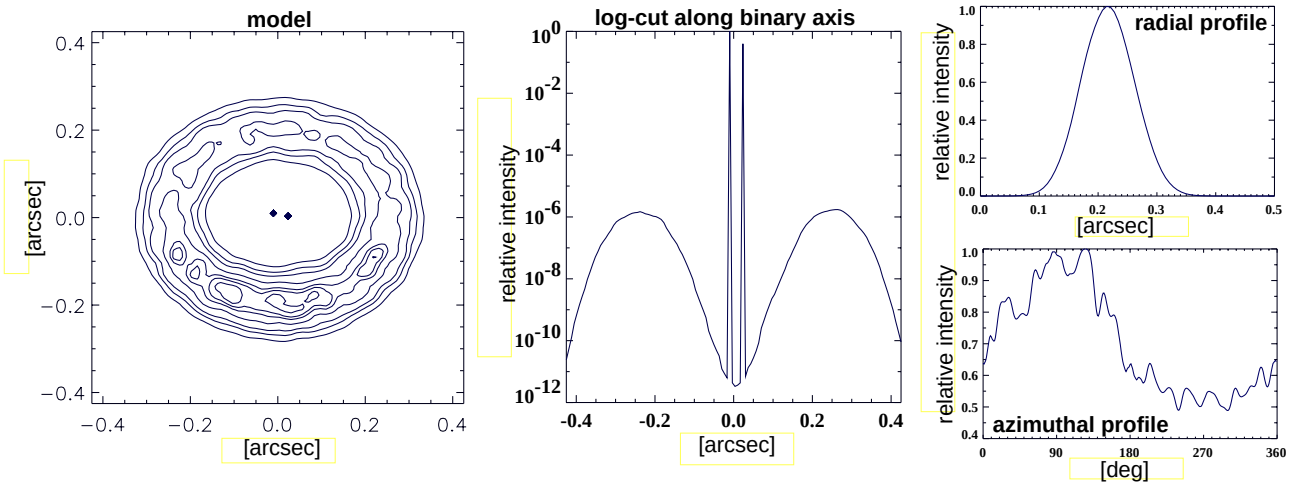

Fig. 1. The model of young binary star surrounded by its circumbinary ring used for our study. Left: contour plot of the model. The seven level lines correspond respectively to 0.1, 0.2, 0.3, 0.5, 0.7, 0.8 and 0.9 of the maximum value of the circumbinary ring (i.e. respectively 2.6×10^{-7}, 5.3×10^{-7}, 8.0×10^{-7}, 1.3×10^{-6}, 1.8×10^{-6}, 2.1×10^{-6}, and 2.4×10^{-6} of the maximum value of the whole object). Center: logarithmic plot of the cut along the binary axis. Up right: radial intensity profile $I_\theta(r)$ of the circumbinary ring. Bottom right: azimuthal intensity profile $I_r(\theta)$ of the circumbinary ring.

represent a young binary object located at a distance of about 2.5 times that of the Taurus-Auriga Complex.

Figure 1 shows different representations of our model. In order to characterize in detail the circumbinary ring we have plotted both its radial intensity profile $I_\theta(r)$, defined as the integration over the polar angle θ of the intensity map $I(\theta, r)$, and its azimuthal intensity profile $I_r(\theta)$, defined as the integration over the radius r of $I(\theta, r)$.

Let us point out that this combination of point-like and diffuse structures with a very high dynamic range between them is a severe test for imaging since, as a consequence of their vicinity, there will be a strong interaction between the image of the core binary star image and that of the circumbinary ring.

2.2. Interferometric PSFs

The spatial sampling adopted for all the interferometric PSFs used in this paper is 3 pixels per Full-Width at Half-Maximum ($FWHM$) of the fringes, where the $FWHM$ is equal to λ/L, with L the total baseline length (22.65 m = 8.25 m effective diameter of each pupil + 14.4 m baseline separation), and λ the filter central wavelength (2.2 μm all along this paper).

Since we intend to study separately the effects of partial angular coverage and partial AO-correction, we will consider different sets of PSFs for each case. When dealing with the angular coverage effect, we will assume perfectly coherenced and cophased PSFs (no optical aberration), while when dealing with the AO-correction effect, we will assume a good angular coverage. We refer to the corresponding sections for further details.

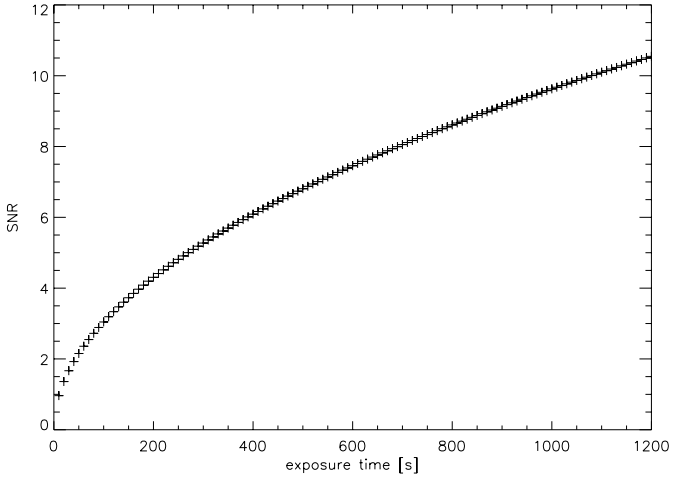

Fig. 2. SNR vs. integration time for the detection of the circumbinary ring.

2.3. Image formation process

Sets of interferometric images are formed by convolving the model with the PSFs of a given set (each PSF corresponding to a given parallactic angle). Sky background emission is added to the results which are eventually corrupted with Poisson and detector noise realizations. The following parameters are used all along this study: a total efficiency (mirror+optics+detector) of 25%, a sky background brightness of 12.5 mag/arcsec^2, and a read-out noise (RON) corresponding to the scientific imaging device of 2 e$^-$ rms.

From the above parameters and the characteristics of the circumbinary ring it is straightforward to compute the expected average SNR of the ring emission as a function of the integration time. Such a function is plotted in Fig. 2. We can in particular observe that 1 min integration time,

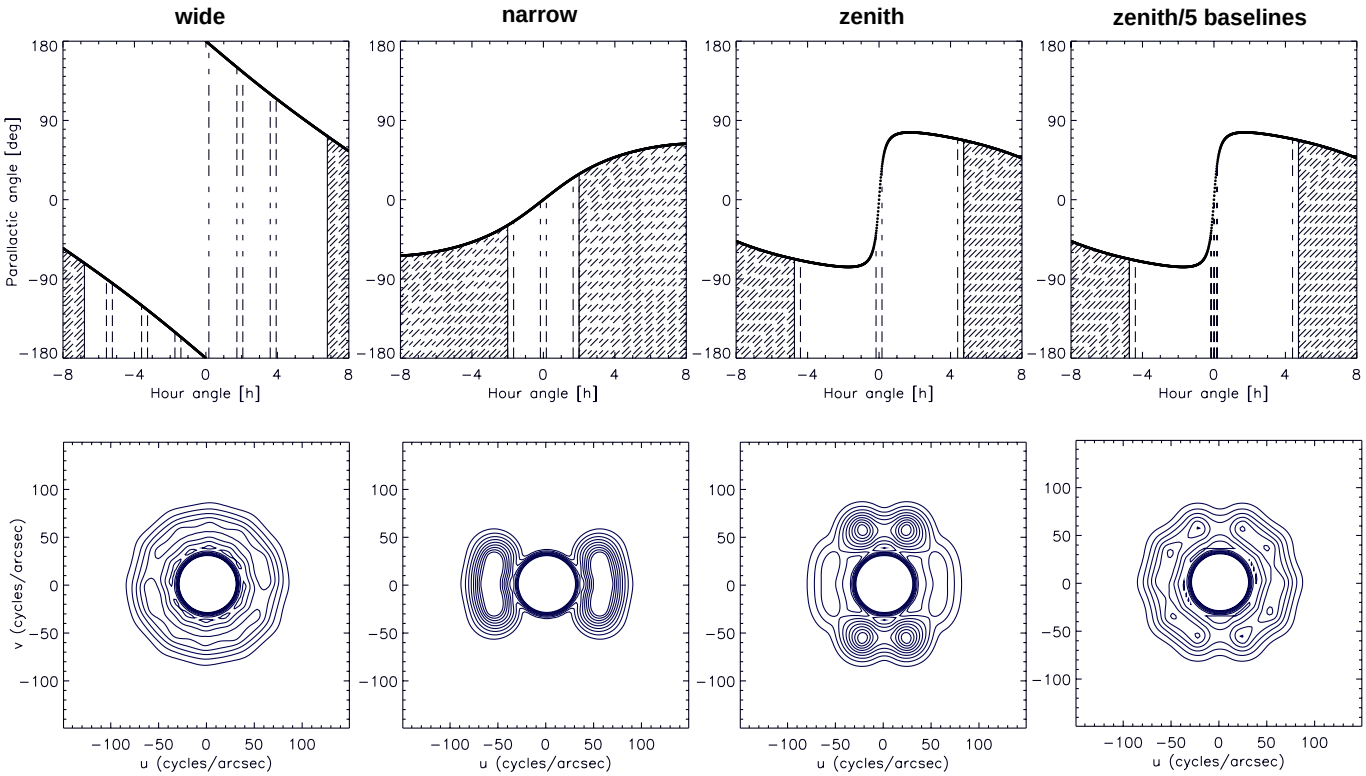

Fig. 3. The four cases of angular coverage considered. First row: plots of the parallactic angle q as a function of the hour angle H for an object of declination δ, from left to right: $+80°$ ("wide" case), $-20°$ ("narrow" case), $+30°$ with 3 baselines ("zenith" case), and $+30°$ with 5 baselines ("zenith/5 baselines" case). The filled regions, accessible only at airmass >2, are not considered in the present study. The intervals defined by the vertical dashed lines represent the variation of the parallactic angle during the considered integration time: 20 min in all cases, but 1 min only for the three central intervals of the "zenith/5 baselines" case. Second row: the corresponding angular coverages in the spatial frequency space represented by means of level lines of the sum of the power spectra of the corresponding PSFs. Ten levels (from 0.01 to 0.1 of the maximum value) are shown.

the shortest exposure-time we are considering, leads to an average SNR of $\sim$2.5, while 20 min, the longest exposure time, leads to an average SNR of $\sim$10.

3. Angular coverage effects

3.1. The cases considered

The parallactic angle q is defined as:

$$q = \arctan\left(\frac{\tan\phi\cos\delta - \sin\delta\cos H}{\sin H}\right), \qquad (1)$$

where ϕ is the latitude of the observatory ($+32.667°$ in the case of LBT), δ the declination of the object, and H the hour angle. Four different cases of variation of the parallactic angle q versus the hour angle H are shown in Fig. 3, each representative of a relevant situation in terms of accessible range of parallactic angle and field-rotation velocity.

The first case (the "wide" case – left-part of Fig. 3) gives the largest range of parallactic angle ($\sim$200°); it corresponds to an object with a declination of $+80°$. The second case (the "narrow" case) gives the smallest range of parallactic angle ($\sim$60°); it corresponds to the angular coverage of an object with a declination of $-20°$. In the two other cases (the "zenith" case and the "zenith/5 baselines" case) the range of parallactic angle ($\sim$135°) is intermediate when compared with the previous ones, but the corresponding field-rotation velocity around $H = 0$ is much higher, due to the fact that the object is much closer to the zenith ($\delta = +30°$).

In order to sample the covered regions of the u–v plane in a way which is approximately uniform for the four cases, we consider six equispaced parallactic angles for the "wide" case, three for the "narrow" case and the "zenith" case, and five for the "zenith/5 baselines" case, as represented in Fig. 3. This corresponds to an angular sampling of roughly one baseline each 30° of parallactic angle.

We consider an integration time of 20 min for each observation (each observation corresponding to one range of parallactic angle) of the first three cases. This corresponds to a variation of parallactic angle of $\sim$5° during each observation of the "wide" case and the "narrow" case (low field-rotation velocity). In the "zenith" case (fast field-rotation velocity) the integration time corresponds to a variation of $\sim$1.5° for the two extreme parallactic angles, and of $\sim$76° for the middle one. Therefore in the "zenith/5 baselines" case we split the latter wide angular-spanning observation into three angularly equispaced short exposures, each one of 1 min integration time (corresponding to a variation of

parallactic angle of ∼5°). In such a way we aim to compare the effect of field-rotation averaging, typical of a long exposure, with the effect of noise increase, arising from the fact that the long exposure is splitted into three shorter ones.

In our simulations the effect of the rotation of the baseline during the integration time ("time-averaging") is taken into account by adding snapshot PSFs of different orientations with a temporal step of 1 min. In addition to this, we also include the width of the K broad-band filter ($\Delta\lambda = 400$ nm), by adding four monochromatic PSFs corresponding to wavelengths within the band. However it has to be noted that in our tests we do not find a significant effect of this kind of further refinement.

We also note that in the "zenith/5 baselines" case the fluxes of the images with different integration times are normalized in such a way that they have the same integrated value, as required by our image restoration algorithm (Bertero & Boccacci 2000a).

We obviously expect the best reconstruction in the first case, since the angular coverage is complete (greater than 180°) and there is no dramatic variation of the parallactic angle during the integration time. At the opposite, the second case corresponds to a limited range of spatial frequencies "seen" during the observations. The third case is characterized by a wide angular averaging due to the fast field-rotation when passing through the zero-hour angle. This phenomenon is reduced in the fourth case, but at the cost of a noise increase.

3.2. Reconstruction of the whole object and estimation of the parameters of the binary star

Figure 4 shows the restorations of the whole object obtained for the four cases of angular coverage we are considering.

Elongation of the small scale features, i.e. the lumpy features and the binary star components, are clearly visible, especially in the "narrow" case and in the "zenith" case. This is due to the incomplete coverage which implies orientations with different resolutions and therefore elongated shapes of the point-source objects. This elongation is, in the "narrow" case, in the direction where the parallactic angles are not sampled and, in the "zenith" case, in the direction where these angles are smeared. The noise amplification due to the three low-SNR baselines of the "zenith/5 baselines" case is also evident in the restored ring. We will return on this phenomenon when treating the restoration of the ring alone. However we observe that, in the "zenith/5 baselines" case, the binary is less elongated than in the "zenith" case. It is also better resolved, as it can be seen from the cuts of the restorations along the axis of the reconstructed core binary star. It is to be noted anyway that in all cases both the core binary star *and* the circumbinary ring are clearly detected.

Let us now investigate quantitatively the effect of the different angular coverages on the restoration of the parameters of the core binary star. In Fig. 5 the errors on these parameters are plotted as functions of the number of OS-EM iterations. We point out that in all cases the parameters converge to the correct values when the number of iterations increases, although in the "wide" case the convergence is globally faster than in the other ones.

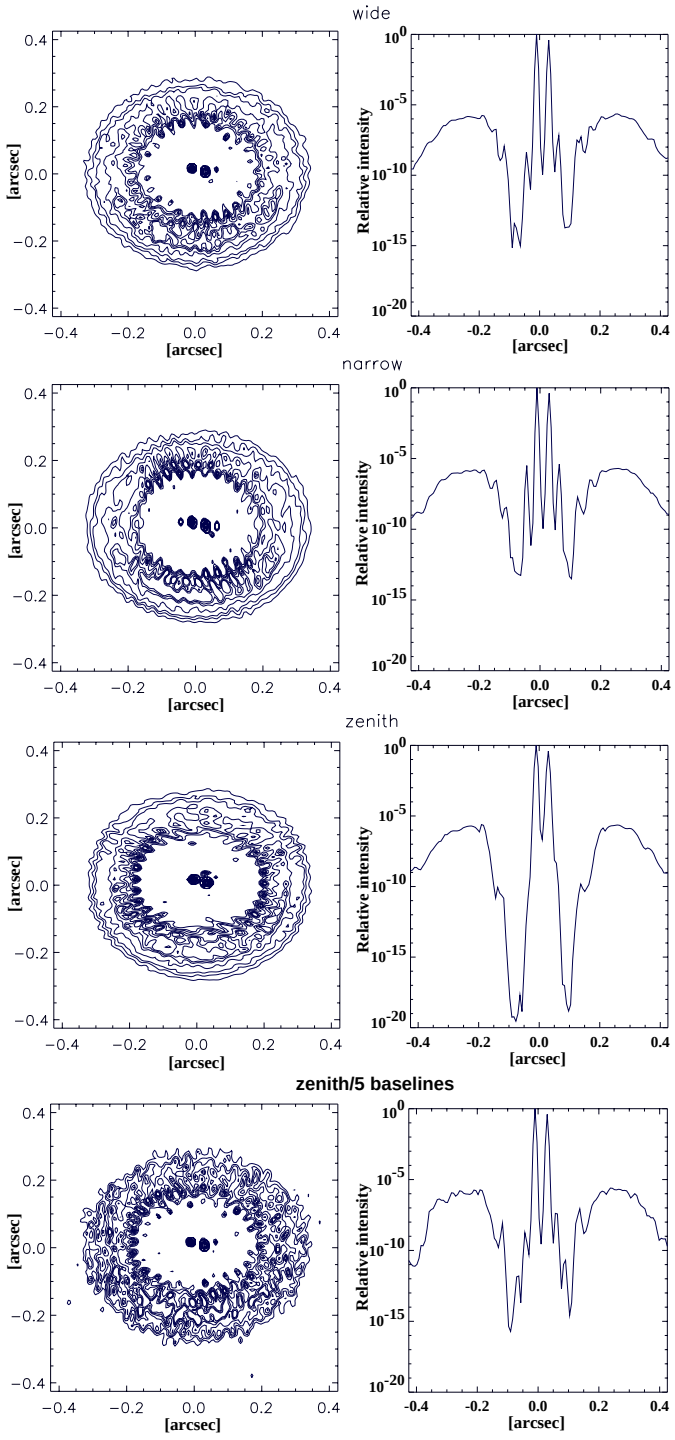

Fig. 4. Restoration of the model of young binary star for the four cases of angular coverage. The reconstructed images are represented with the same levels as in Fig. 1. The logarithmic plots of the cuts along the axis of the reconstructed binary star are also shown.

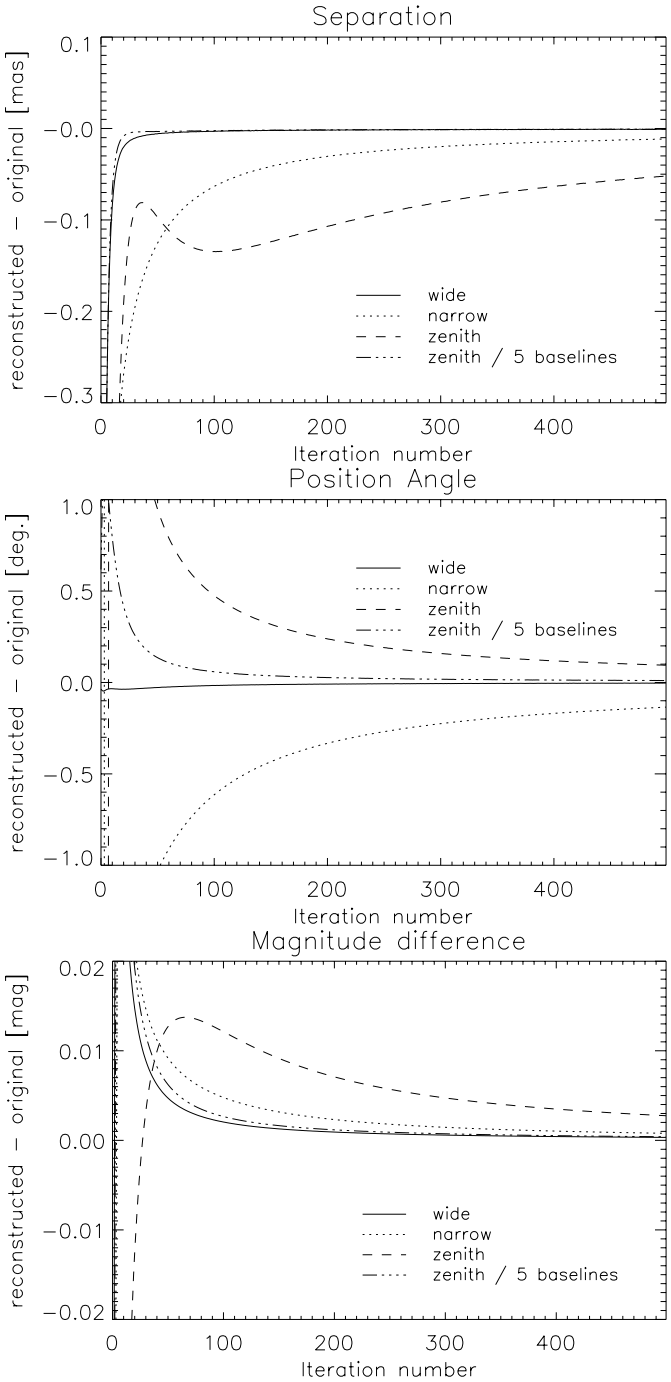

Fig. 5. Restoration of the parameters of the binary star: plots of the errors as functions of the number of OS-EM iterations for the restoration of the angular separation ρ, the position angle PA and the difference in magnitude Δm, and for the four cases of angular coverage.

In addition the accuracy in the retrieval both of the astrometric parameters (ρ and PA) and of the photometric parameter Δm is definitely better when the coverage is complete ("wide" case), or almost complete without wide time-averaging ("zenith/5 baselines" case). We also observe that the direction of the axis of the binary star falls in the "well-scanned" angular sector of the first two cases while it is within the angular smeared region of the third case. As a consequence in the "zenith" case the retrieved separation is smaller than the correct one (the elongation lies in the direction of separation).

Note that from the point of view of (relative) astrometry and photometry the absolute errors are remarkably small (error on $\rho \lesssim 0.05$ mas, error on $\Delta m \lesssim 0.005$ mag).

3.3. Circumbinary ring restoration

For the evaluation of the restoration of the circumbinary ring, we adopt the following approach: a masking of the central core is performed on the different reconstructed images so that the radial profile $I_\theta(r)$ and the azimuthal profile $I_r(\theta)$ can be easily computed; then, if we denote by $\boldsymbol{I}$ the vector formed by the samples of the radial or azimuthal profile of the original model and by $\boldsymbol{I}^{(k)}$ the corresponding vector obtained from the result of the kth iteration, the accuracy of the restoration provided by such an iteration is measured by computing the following relative distance:

$$R_I^{(k)} = \frac{\|\boldsymbol{I}^{(k)} - \boldsymbol{I}\|}{\|\boldsymbol{I}\|}, \tag{2}$$

where the norm is the Euclidean one, i.e. the square root of the sum of the squares of the sample values.

Besides the reconstruction of the whole model, we also consider a second approach which consists in applying the restoration method to data obtained after subtraction of the binary star contribution. A possible procedure could be the following: first perform a deconvolution of the complete data to estimate the binary parameters (as performed in Sect. 3.2); next subtract from the original data the binary images obtained by convolving the estimated binary with the PSFs; finally perform a second deconvolution of the circumbinary data alone. Even if this kind of procedure is routinely applied with success for probing the circumstellar environment of T-Tauri stars and possibly detecting disks emission (see e.g. Roddier et al. 1996; Krist et al. 2000), its practical implementation and validation are beyond the scope of this paper. Therefore we only consider a perfect subtraction of the binary contribution. In other words we perform the restoration of the circumbinary ring alone and then compute again $R_I^{(k)}$ on both the radial and azimuthal profiles. This last procedure has also the advantage that it provides further information on the behavior of our restoration method when applied to faint diffuse objects (see Paper I).

Figure 6 shows the results of the restoration of the ring alone, while the relative distances $R^{(k)}$ for the four cases of angular coverage and the two approaches considered (restoration of the complete object and of the ring alone) are shown in Fig. 7.

As concerns the maps of the restored ring, a simple visual analysis and comparison with the model of Fig. 1 makes already evident that when the angular coverage increases (from the "narrow" case to the "wide" case through the "zenith" case), the reconstructed features

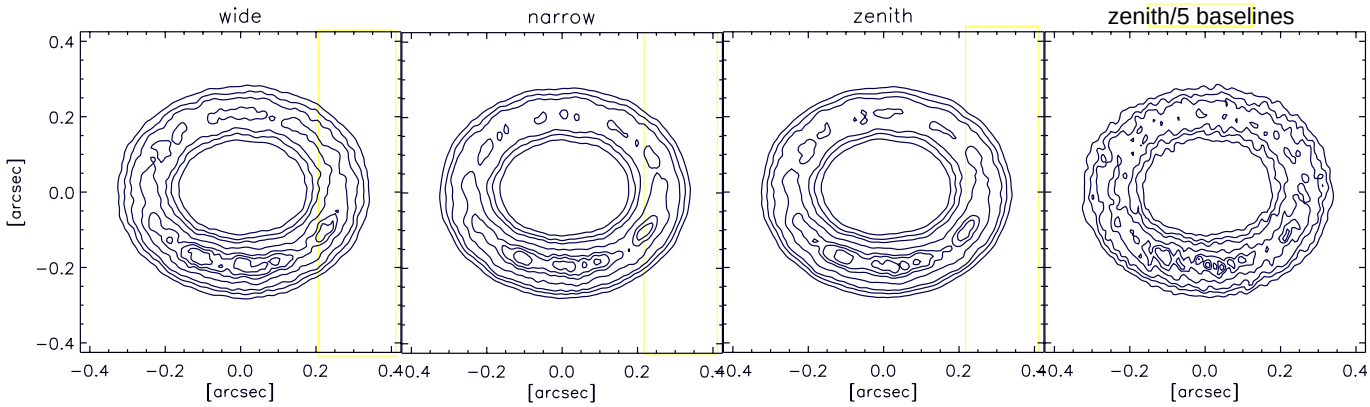

Fig. 6. Restoration of the circumbinary ring after binary subtraction for the four cases of angular coverage. The level lines correspond to 0.1, 0.2, 0.3, 0.5, 0.7, 0.8, and 0.9 of the maximum value of the model, and therefore are equivalent to the level lines of Fig. 1.

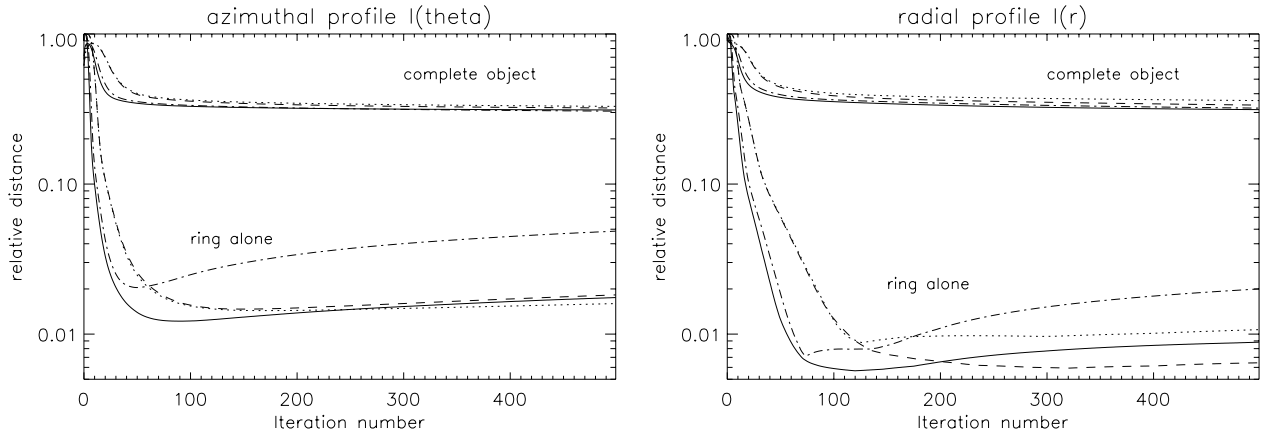

Fig. 7. Circumbinary ring restoration: logarithmic plot of the relative errors in the restoration of the azimuthal profile $I_r(\theta)$ (left) and of the radial profile $I_\theta(r)$ (right), in the four cases of angular coverage. Continuous line is for the "wide" case, dotted-line for the "narrow" case, dashed line for the "zenith" case, and dashed-dotted line for the "zenith/5 baselines" case. Two sets of results are represented: the upper set corresponds to the restoration of the complete object, while the lower set corresponds to the restoration of the ring alone.

become sharper. In addition, the "zenith/5 baselines" case clearly shows the expected effect of noise increase.

This is quantitatively confirmed by Fig. 7, where the common behavior of the various distance curves is a minimum around 100–200 iterations. This feature is known in the theory of iterative methods for image restoration as *semiconvergence* (see e.g. Bertero & Boccacci 1998, as well as Paper I), and is due to the phenomenon of *noise amplification* (see also White 1994). Moreover, as it is known, this phenomenon is stronger in the case of noisier data, in the sense that the optimal number of iterations decreases with increasing noise. This last point is evident here from Fig. 7 when comparing the "zenith" case with respect to the "zenith/5 baselines" case.

3.4. Discussion

A first result of our analysis is that, as expected, the restored image has a higher quality when a broader range of parallactic angles is accessible. However the influence on the extended part of our model is not dramatic: reliable results are obtained even in the case of incomplete angular coverage or smeared baselines.

The interpretation of this effect in the u–v plane is as follows: the spectrum of the extended part is mainly concentrated at low angular frequencies so that the information provided by a single mirror is fundamental while that coming from the long baseline provided by the interference between the two mirrors is not very relevant.

More critical is the effect on small features or on point objects such as the stars of the binary. Indeed their spectrum extends outside the disc in the u–v plane covered by a single mirror so that, in the case of incomplete coverage, the restorations exhibit elongated shapes in the directions not covered by the baselines. It is interesting to remark, however, that, as concerns the estimation of the binary parameters the main difference between the different cases consists essentially in different convergence rates. The final accuracy is always quite good even if we show that an improvement can be obtained by splitting a too large angular smearing into shorter exposures.

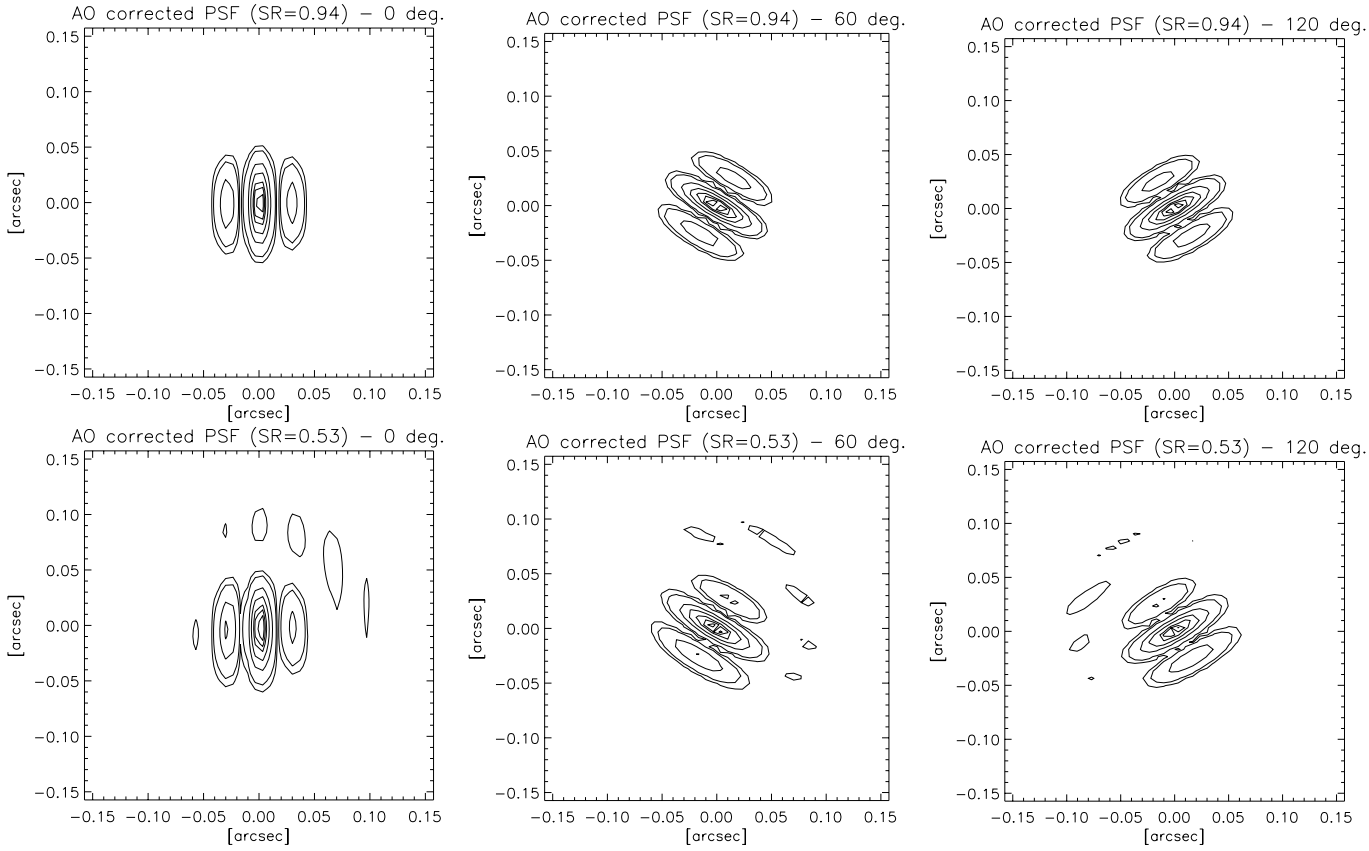

Fig. 8. Two examples of the sets of interferometric AO-corrected PSFs used in this study. Each set consists of three PSFs corresponding to three equispaced orientations of the baseline (0°, 60°, and 120°). The average SR of the upper set is 0.94, and 0.53 for the bottom set. Level lines correspond to 0.05, 0.1, 0.3, 0.5, 0.7, 0.8, and 0.9 of the maximum value.

The last strategy can be hardly applied to the faintest objects due to the need of finding a compromise between integration time and time-smearing. In particular we find that, if some images have poor SNR values, the result may be corrupted by the phenomenon of noise amplification. In such a case the choice of the number of iterations is more critical and we conclude that the definition of a reliable stopping-rule (see Lanteri et al. 1999a, 1999b) will be required when dealing with real data.

4. Partial AO-correction effects

Although the goal of AO is to correct the atmospheric degradations as perfectly as possible, it is obvious that residuals will always be present and have a relative destructive effect on image formation.

The effects of partial correction on each single pupil of an interferometer have the global consequence that the image of a point-source is not exactly an Airy disc, but consists of a central core surrounded by a halo, where typically the first Airy ring is visible but broken. The tip-tilt residual causes a residual global image motion, while the high-orders residuals tend to "speckle-ize" the image.

In the interferometric case, the dilution of the pupil implies that differential effects must also be considered. The residual of differential piston tends to produce a motion of the fringes pattern along the baseline axis. In addition to it, the differential tip-tilt, resulting from both the tip-tilt residuals of the single pupils, has the effect of a bad superimposition of the two single-pupil PSF envelopes: the envelopes from the two pupils combine in a deformed one. Hence the effect on the fringes is similar to that due to the differential piston, but with the main difference that the central fringe remains static, while in the case of differential piston the central fringe is moved.

For what concerns the high-orders residuals, and as in the case of single-pupil astronomy, they cause the interferometric PSF to be composed of a central fringed core together with a "speckle-ized" halo where each speckle-like feature is fringed as well. In the following of this section we consider the overall deformation of the PSFs due to the whole ensemble of perturbations.

4.1. The AO-corrected interferometric PSFs

When dealing with the deconvolution of post-AO images, an important issue is the good estimation of the PSF that best corresponds to the observed object. Mainly due to the anisoplanatism error that affects the AO correction of an object distant by a certain angle from the guide star (GS), its PSF can be very different from the GS one. By extension the PSF related to the formation of the image of the observed object (the "object PSF") can be very different

from the PSF related to the point-like reference star used for deconvolution (the "reference PSF"). Note that the reference point-like star is not a priori the GS used for the AO correction (or one of the GS' in the case of MCAO).

In the following of this paper we use five different sets of PSFs, obtained by simulating the behavior of the LBT AO system in its single-reference single-conjugate mode (i.e. classical AO), and using the Software Package CAOS (Carbillet et al. 2001a). Two typical examples of our sets of PSFs are shown in Fig. 8.

As in the case reported in details in Carbillet et al. (2000), we simulate our sets of AO-corrected interferometric PSFs for three parallactic angles: 0°, 60°, and 120°. Note that this angular coverage of the frequency plane is good enough to allow us to focus on the AO-correction effects only. The simulations are performed in closed-loop with an independent realization of the turbulent atmosphere for each parallactic angle. This will be the situation in real life since different parallactic angles correspond to different instant during the observation night (see Sect. 3). The scope of the present section being to study the effects due to the difference between the reference PSFs and the object PSFs, we simulate several sets of PSFs by taking point-like stars with different off-axis angles (the GS is considered on-axis), varying from 0 arcsec towards the isoplanatic angle corresponding to the simulated atmosphere (depending on the turbulence profile, the wavefront outer-scale, and the speed of each turbulent layer). We then characterize the corresponding image quality by means of the resulting Strehl ratio (SR), defined as the ratio between the intensity of the AO-compensated PSF and the intensity of the ideal PSF, measured in the central point of the later. The resulting SR are respectively: 0.94 (on-axis PSF), 0.93, 0.88, 0.81, and 0.53 (farthest PSF).

All along this section we characterize the quality of the correction of a given set of PSFs by its SR only. Although a full description of each PSF would require also parameters such as its $FWHM$ and its encircled energy (both related to the attained resolution), as well as the main features of its morphology (mainly for what concerns the halo), we assume here that the SR is sufficient to characterize the PSFs, and that a different SR implies a different $FWHM$ and a different morphology. This assumption is reasonable also because we are dealing here with relatively high SR (>50%).

Our first application concerns classical AO. Therefore we assume in the following that the reference star used for deconvolution corresponds to the AO GS (and hence that the SR of the reference PSFs is 0.94), while we consider four cases of object PSFs corresponding to the SRs from 0.93 to 0.53. We have considered here anisoplanatism only, but other sources exists, such as anisopistonism (Esposito et al. 2000; Femenía et al. 2001), but also the geometry and magnitude map of the asterisms of the GSs when considering an MCAO scheme. Therefore we call the "general AO case" this first application, because it also includes MCAO when the correction is not perfectly uniform.

In addition to it, we also consider a second application concerning a uniform MCAO system. Indeed, the main attractive feature of this kind of system is its expected capability of maintaining the same level of correction all over the corrected FoV. In good conditions the PSFs are typically expected to be stable over a FoV of up ∼2 arcmin (see e.g. the recent results reported in Bello et al. 2001 or Carbillet et al. 2001b). Since the AO-correction quality depends, as in the classical case, on the atmospheric and system status during the single observation, our MCAO case study concerns different levels of correction over a FoV covering both the astronomical object and the reference star. For the sake of simplicity we limit our analysis to the best situation ($SR = 0.94$ for both the reference PSFs and the object PSFs), and to the worst one ($SR = 0.53$ for both sets). We call this second application the "uniform MCAO case".

4.2. General AO case

Four sets of LBT images are generated by convolving the model of Sect. 2.1 with the four sets of PSFs corresponding to the four SR values indicated before (object PSFs) and by adding to the results sky background emission and noises as defined in Sect. 2.3. Next the four sets of images are deconvolved using the reference PSFs. The restoration of the binary star is again evaluated in terms of the retrieval of its parameters ρ, PA, and Δm, after deconvolution of the whole object, while the restoration of the circumbinary ring is still evaluated in terms of the retrieval of its azimuthal profile $I_r(\theta)$ and its radial profile $I_\theta(r)$.

Figure 9 shows the results obtained for the binary parameters, in the four SR cases. A first conclusion which can be derived from these plots is that all parameters are remarkably retrieved, for all cases of SR. In particular, if we first consider the plots of the magnitude difference, we find that the different SR cases lead to different errors, from almost zero (case of $SR = 0.93$) to less than 0.07 mag. (case of $SR = 0.53$). The main difference between the four cases consists in different and slightly wrong estimated values of Δm rather than in different convergence rates. On the other hand, the PA plots show that in the cases with $SR = 0.53$, 0.81 and 0.88 the results converge toward the same value (with a final error of a few hundredth of degree only) but at very different rates. The case $SR = 0.93$ is again almost perfect here, converging to the right value in less than 100 iterations. Finally the separation plots show the same behavior as those for Δm, but with a difference between the cases with $SR = 0.81$ and $SR = 0.88$, more similar to the behavior of the PA plots. Note that the final error for ρ is at most ∼0.25 mas for the worst case scenario ($SR = 0.53$), which is still remarkably small.

As concerns the evaluation of the restoration of the circumbinary ring, we have adopted again the two different approaches mentioned in Sect. 3. As it is shown by the upper plots of Fig. 10, the reconstruction of the ring

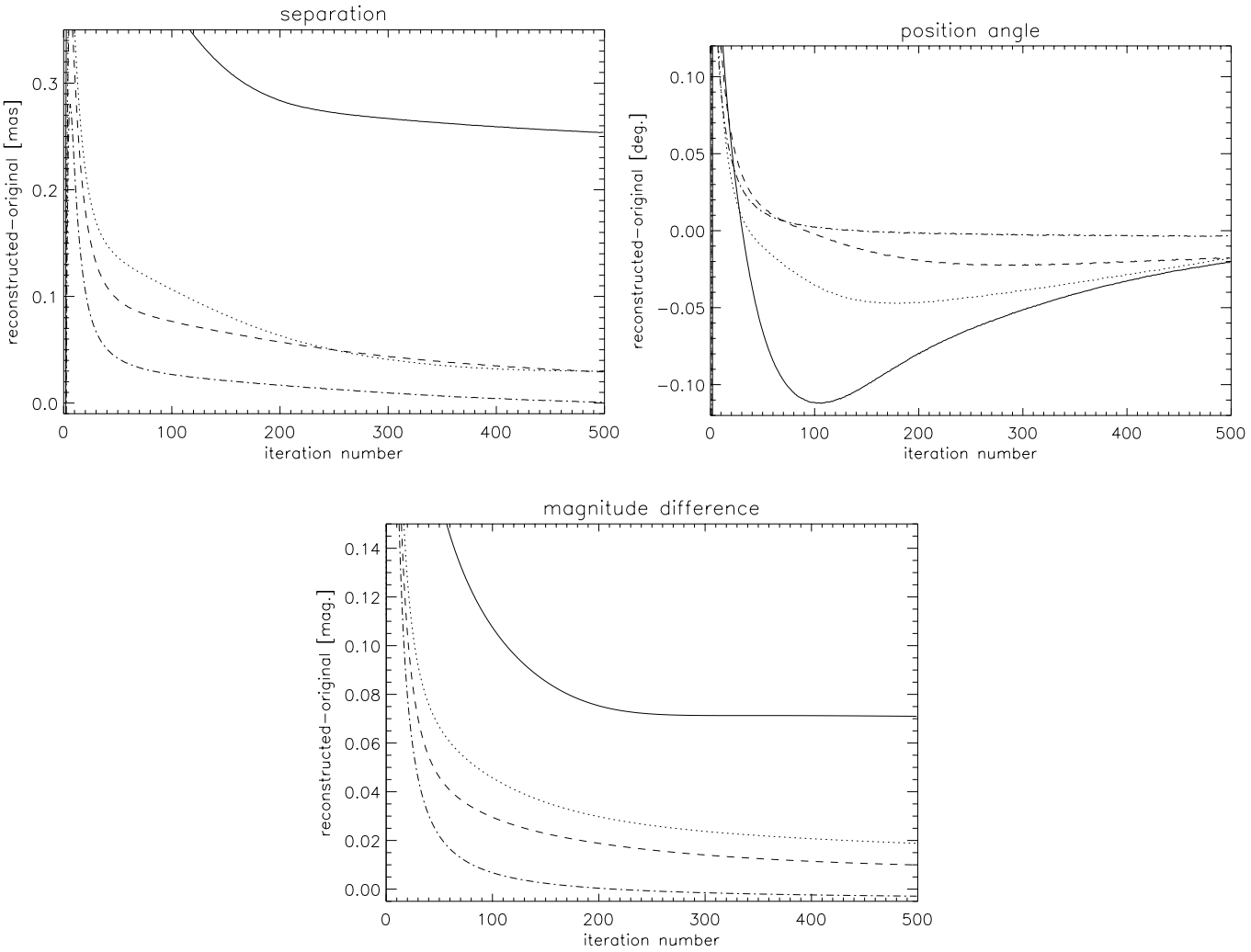

Fig. 9. Restoration of the binary parameters – general AO case: error plots for the separation ρ, position angle PA, and magnitude difference Δm, as functions of the number of OS-EM iterations for the four SR cases. Continuous line is for $SR = 0.53$, dotted line for $SR = 0.81$, dashed line for $SR = 0.88$, and dashed-dotted line for $SR = 0.93$.

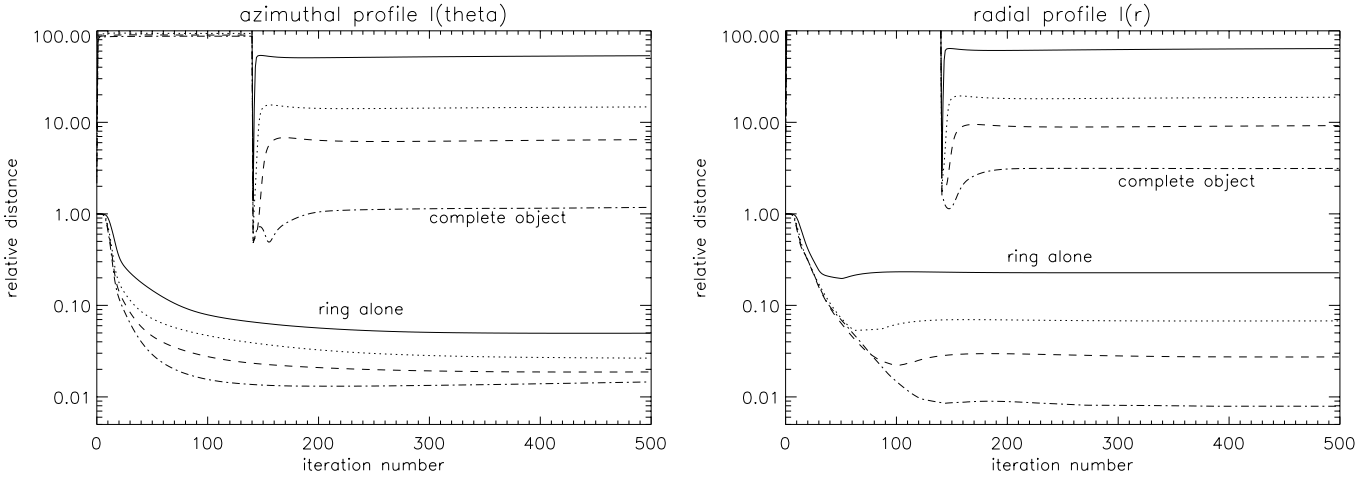

Fig. 10. Restoration of the circumbinary ring parameters – general AO case: logarithmic plots of the relative restoration error on the azimuthal profile $I_r(\theta)$ (left) and on the radial profile $I_\theta(r)$ (right), for the four SR cases. Continuous line is for $SR = 0.53$, dotted-line for $SR = 0.81$, dashed line for $SR = 0.88$, and dashed-dotted line for $SR = 0.93$. Two sets of results are represented: the upper set corresponds to the deconvolution of the data of the complete object, while the bottom set to the deconvolution of the ring data.

as obtained from the complete object data is not satisfactory, while the reconstruction process applied to the subtracted data provides good results. This result underlines the fact that a good PSF-subtraction method will be necessary when dealing with real data of this kind of object. The different values of SR clearly lead to different levels of precision in the restoration of the two profiles, even if the differences are more evident in the case of the radial profile $I_\theta(r)$. In this case, indeed, the final error ranges from ∼20% for the case of $SR = 0.53$, to less than 1% for the $SR = 0.93$ case. For $I_r(\theta)$ the range of error is smaller: from 5% to 1.5%. It is also interesting to point out that in all cases the algorithm converges after about 100–200 iterations.

The overall good accuracy in the reconstruction of the ring is confirmed by Fig. 11 where the reconstructed images are given. While in the case of $SR = 0.53$ the principal features of the ring are already recovered, in the other cases it is also possible to recognize almost all details of the model represented in Fig. 1.

4.3. Uniform MCAO case

In this second application we assume a MCAO system which allows an ideal uniformity of the PSFs over the whole reconstructed FoV. We point out that such a system would not only assure a remarkable similarity between the reference and object PSFs, but would also make easier the search for a suitable reference star since any star in the field can be used. Therefore we simulate such a situation by considering two of the sets of images generated in the previous section (and precisely those corresponding to $SR = 0.94$ and 0.53), and by deconvolving these sets by means of the same PSFs used for their generation.

Figure 12 shows the results obtained for the reconstruction of the binary parameters in the two MCAO cases considered. Note that, for an easier comparison, these plots have the same identical range as those of Fig. 9.

A comparison with the results obtained in the general AO case clearly shows that the possibility of having reference PSFs as similar as possible to the object PSFs greatly improves the precision of the results. No more significant offsets are visible in these curves that almost perfectly converge toward the correct solution, in the case of $SR = 0.94$ as well as in the case of $SR = 0.53$. Especially in this last case, the comparison with the plots of Fig. 9 shows that a better precision *and* a faster convergence are obtained when the similarity between the reference PSFs and the object PSFs is preferred with respect to the choice of a set of reference PSFs better corrected, but different from the object PSFs. The main difference due to a different quality of the global AO-correction consists in a different convergence rate, which is slower in the case of $SR = 0.53$ than in the case of $SR = 0.94$, with a final error which in all cases clearly tends to zero.

As concerns the restoration of the circumbinary ring, the error plots of Fig. 13 for the radial and azimuthal profiles have approximately the same behavior as those for the binary parameters. Here again the comparison with the general AO case shows the great advantage of PSF uniformity. Furthermore it is to be noted that even when deconvolving the whole object, with the already underlined problem of huge dynamic range between the ring and the core binary star, the results on the retrieval of $I_\theta(r)$ and $I_r(\theta)$ are better than those obtained in the general AO case, especially for what concerns the azimuthal profile.

Table 1. Relative distances between the profiles of the incoherent sums of images and those of the model.

Strehl case	rel. dist. on $I_\theta(r)$	rel. dist. on $I_r(\theta)$
0.53	0.33	0.062
0.94	0.19	0.034

It is interesting to compare also the retrieved parameters with those obtained by taking as ring image the incoherent sum of the three interferometric ring images (obtained at the three parallactic angles). In such a way we can directly evaluate the advantage of using the restoration method. The comparison is performed by computing the relative distance between the radial and azimuthal profiles of the incoherent sums and those of the original model. The results are reported in Table 1 and show that the use of the restoration algorithm provides a much better precision, and that this is already true after a few iterations (∼20 in all cases). A visual confirmation of such a result is shown in Fig. 14, where the reconstructed images are represented in both cases of MCAO correction, together with the corresponding incoherent sums. The great resolution achieved in the reconstructed images is evident.

4.4. Discussion

The results described in this section show the importance of having uniform PSFs over the field even with a lower SR, rather than reference PSFs with a high SR but different from the PSFs in other domains of the field. In other words, this means that when designing and/or using an MCAO system, the uniformity of the PSF seems to be more important than its mean value over the corrected FoV. We have shown in fact that, at least from the point of view of our restoration method, and for the range of relatively high SR values we have simulated, it is more convenient to have a SR of ∼50% stable over the FoV than a SR whose average value is higher but with significant variations over the FoV.

We should anyway mention that a possible solution to achieve the same level of precision and convergence rate in the general AO case could be the use of blind deconvolution techniques (see e.g. Jefferies & Christou 1993; Fusco et al. 1999).

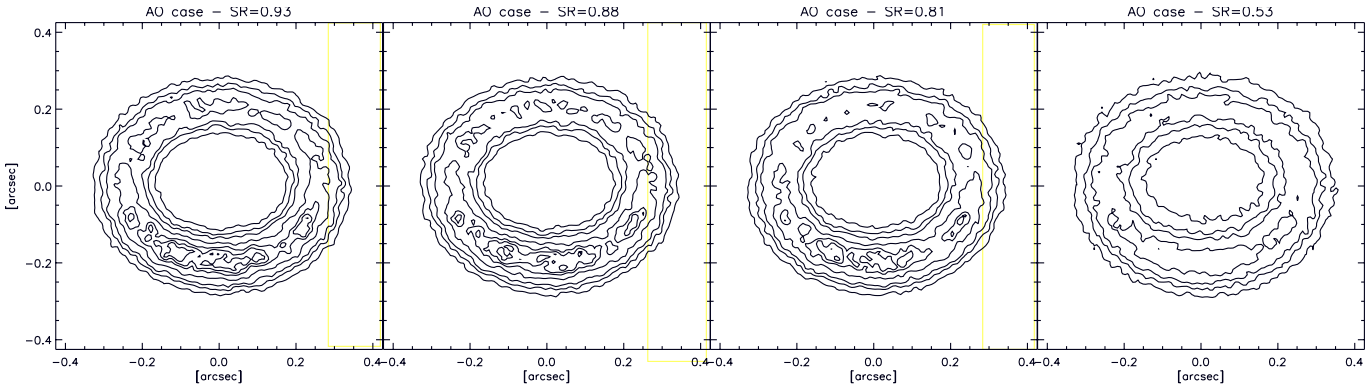

Fig. 11. Restoration of the circumbinary ring – general AO case. The level lines correspond to 0.1, 0.2, 0.3, 0.5, 0.7, 0.8 and 0.9 of the maximum value of the model, and therefore are equivalent to the the level lines of Fig. 1.

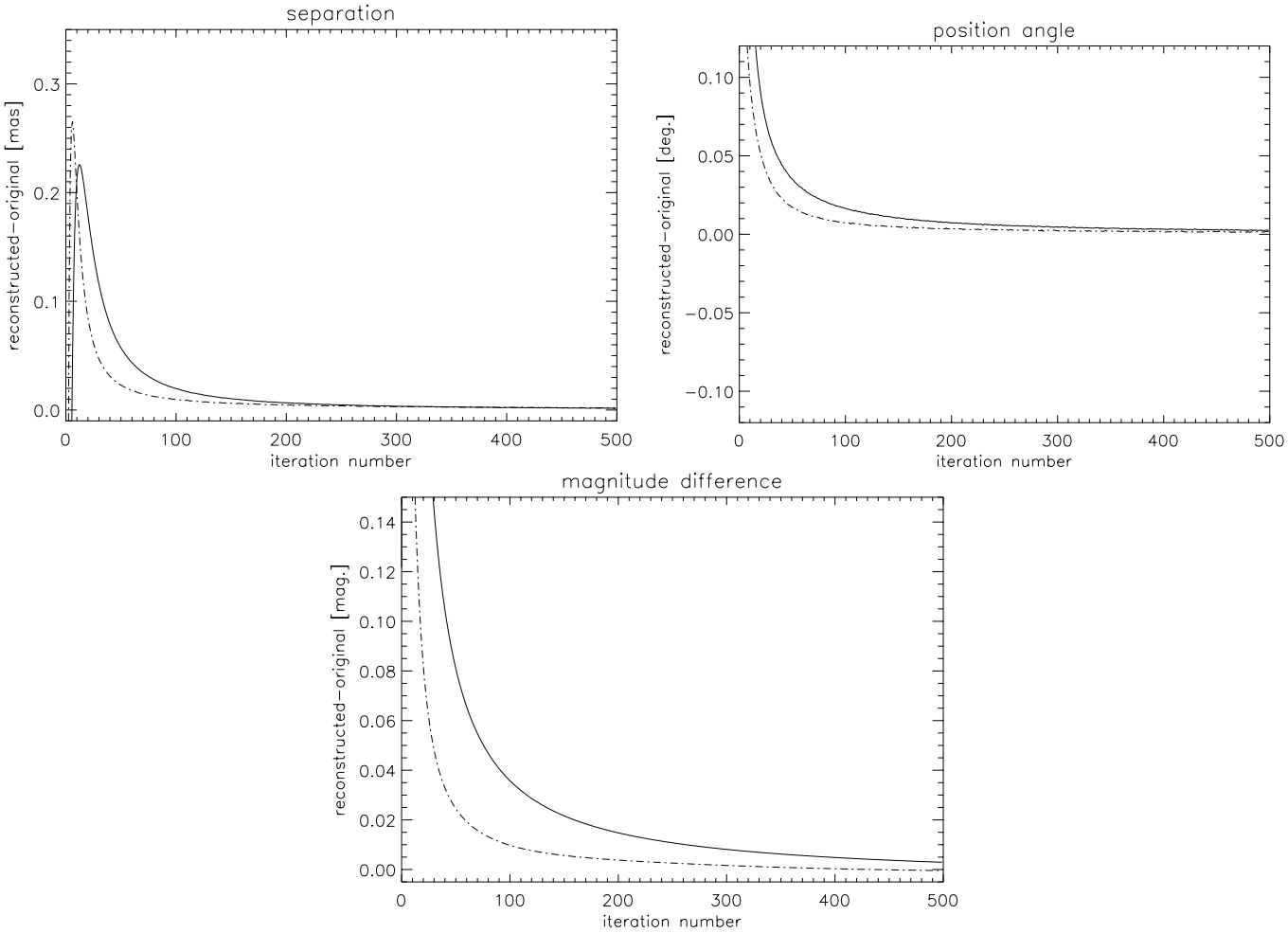

Fig. 12. Restoration of the binary parameters – uniform MCAO case: error plots for the separation ρ, position angle PA, and magnitude difference Δm, as functions of the number of OS-EM iterations for the two SR cases. Continuous line is for $SR = 0.53$, while dashed-dotted line is for $SR = 0.94$.

5. Summary and concluding remarks

In this paper we have applied the first release of the Software Package AIRY (Astronomical Image Restoration in interferometrY) to the case-study of the LBT interferometer. In order to test the interferometric imaging capabilities of LBT we have considered a realistic object: a young binary star surrounded by a faint circumbinary ring. In such a case we have investigated the effect of limited angular coverage and time-averaging smearing on the restored image. Next we have considered the effect of partial AO correction in both cases of general AO and uniform MCAO.

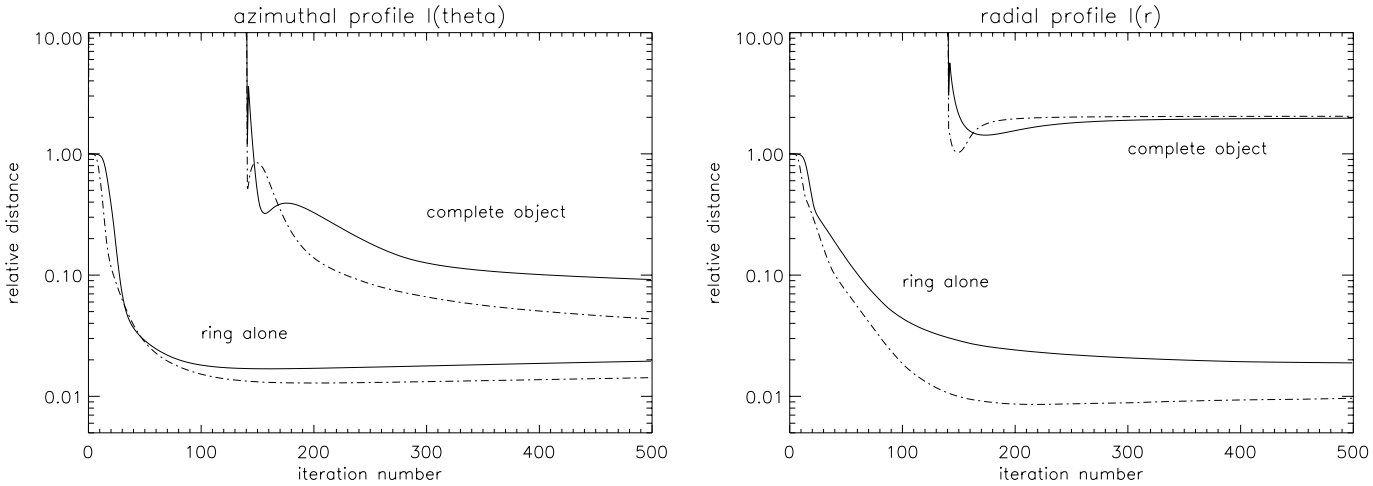

Fig. 13. Restoration of the circumbinary ring parameters – uniform MCAO case: logarithmic plots of the relative restoration error on the azimuthal profile $I_r(\theta)$ (left) and on the radial profile $I_\theta(r)$ (right), for the two SR cases. Continuous line is for $SR = 0.53$, while dashed-dotted line is for $SR = 0.94$. Two sets of results are represented: the upper set corresponds to the deconvolution of the data of the complete object, while the bottom set corresponds to the deconvolution of the ring data.

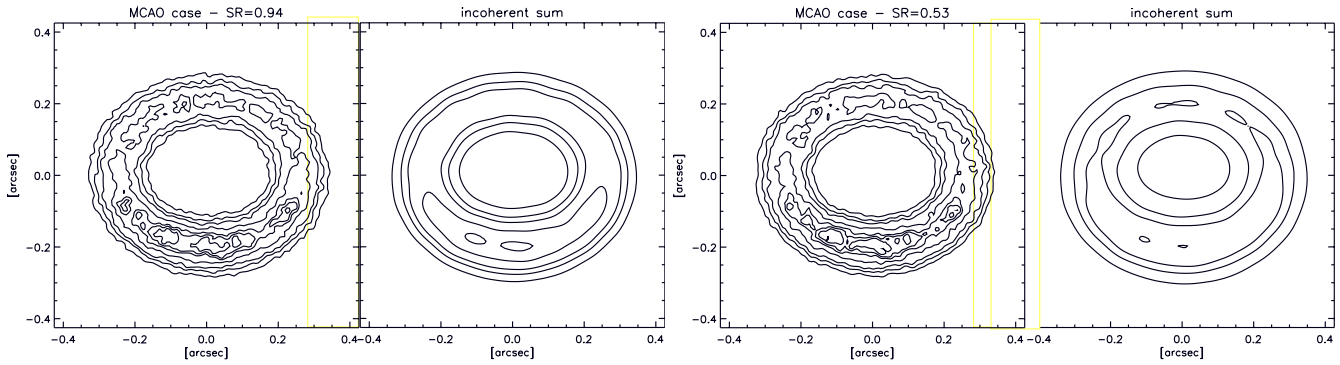

Fig. 14. Restoration of the circumbinary ring – uniform MCAO case. From left to right: the result obtained for $SR = 0.94$ and the corresponding incoherent sum; the result obtained for $SR = 0.53$ and the corresponding incoherent sum. The level lines correspond to 0.1, 0.2, 0.3, 0.5, 0.7, 0.8 and 0.9 of the maximum value of the model, and therefore are equivalent to the level lines of Fig. 1.

We have found that the method intrinsically allows for high-dynamic range imaging. The angular coverage and smearing seems, at the light of the simulations performed, not to affect significantly the large structure of the image nor the parameters of the binary, but only the convergence rate of the iterative method.

For what concerns general AO, we identify a possible direction of investigation in order to overcome the problem of PSF calibration, namely the development and testing of blind deconvolution methods. On the other hand, we have shown that the stability of the PSFs is a main issue for this observational technique, even at the cost of a lower average SR, at least for the field of application we have considered.

Such a condition, which may be satisfied by an MCAO system, is also required by the model of image formation assumed in the deconvolution method (see Paper I, Eq. (1)) and implies that the PSF obtained from a reference star provides a good approximation of the PSF which must be used in the process of image restoration. In addition our results show that, even in the case of relatively low SR, the AO-corrected PSF provides sufficient information at the higher angular frequencies which are accessible in the u–v plane.

Acknowledgements. All the work presented in this paper was done with the help of the Software Package AIRY, version 1.0, and the Software Package CAOS, version 3.0. The Software Package AIRY is obtainable under request and subscription to its dedicated mailing-list by visiting the web site `http://dirac.disi.unige.it`. The Software Package CAOS is obtainable under request and subscription to its dedicated mailing-list by visiting the web site `http://www.arcetri.astro.it/caos`. Both software packages are delivered together with the CAOS Application Builder (version 3.0): the IDL-based graphical environment within which they were developed.

We thank Piero Ranfagni for his help in astrometry, Piero Salinari for several stimulating discussions, Elena Masciadri for useful comments on the manuscript, and Luca Fini for the graphical tools of AIRY and CAOS. This work was also partially funded by CNAA (Consorzio Nazionale per l'Astronomia e l'Astrofisica) under the contract No. 16/97.

References

Bello, D., Conan, R., Le Roux, B., et al. 2001, in ESO Proc. Beyond Conventional Adaptive Optics, ed. É. Vernet, R. Ragazzoni, S. Esposito, & N. Hubin

Bertero, M., & Boccacci, P. 1998, Introduction to Inverse Problems in Imaging (IOP Publishing, Bristol)

Bertero, M., & Boccacci, P. 2000a, A&AS, 144, 181

Bertero, M., & Boccacci, P. 2000b, A&AS, 147, 323

Carbillet, M., Correia, S., Femenía, B., & Riccardi, A. 2000, in SPIE Conf. Ser. 4007, Adaptive Optical Systems Technology, ed. P. L. Wizinowich, 155

Carbillet, M., Fini, L., Femenía, B., et al. 2001a, in ASP Conf. Ser. ADASS X, ed. F. A. Primini, & F. R. Harnden, 249

Carbillet, M., Femenía, B., Esposito, S., Brusa, G., & Correia, S. 2001b, in ESO Proc. Beyond Conventional Adaptive Optics, ed. É. Vernet, R. Ragazzoni, S. Esposito, & N. Hubin

Correia, S., Carbillet, M., Richichi, A., Bertero, M., & Boccacci, P. 2000, in SPIE Proc. 4006, Interferometry in Optical Astronomy, ed. P. J. Léna, & A. Quirrenbach, 650

Correia, S., Carbillet, M., Fini, et al. 2001, in ASP Conf. Ser. ADASS X, ed. F. A. Primini, & F. R. Harnden, 404

Correia, S., Carbillet, M., Boccacci, P., & Bertero, M. 2002, A&A, 387, 733

Esposito, S., Riccardi, A., & Femenía, B. 2000, A&A, 353, L29

Femenía, B., Carbillet, M., Esposito, S., & Riccardi, A. 2000, in SPIE Proc. 4006, Interferometry in Optical Astronomy, ed. P. J. Léna, & A. Quirrenbach, 1116

Fini, L., Carbillet, M., & Riccardi, A. 2001, in ASP Conf. Ser. ADASS X, ed. F. A. Primini, & F. R. Harnden, 253

Fusco, T., Véran, J. P., Conan, J. M., & Mugnier, L. M. 1999, A&AS, 134, 193

Ghez, A. M., White, R. S., & Simon, M. 1997, ApJ, 490, 353

Jefferies, S. M., & Christou, J. C. 1993, ApJ, 415, 862

Krist, J. E., Stapelfeldt, K. R., Menard, F., Padgett, D. L., & Burrows, C. J. 2000, ApJ, 538, 793

Lanteri, H., Soummer, R., & Aime, C. 1999, A&AS, 140, 235

Lanteri, H., Roche, M., Cuevas, O., & Aime, C. 1999, in SPIE Proc. 3866, Optics in Atmospheric Propagation & Adaptive Systems III, ed. A. Kohle, & J. D. Gonglewski, 144

Roddier, C., Roddier, F., Northcott, M. J., Graves, J. E., & Jim, K. 1996, ApJ, 463, 326

Shepp, L. A., & Vardi, Y. 1982, IEEE Trans. Med. Imaging MI-1, 113

White R. L. 1994, in The Restoration of HST Images and Spectra II. Space Telescope Science Institute, ed. R. J. Hanish, & R. L. White, 104

Wood, K., Crosas, M., & Ghez, A. 1999, ApJ, 516, 335